Lithuanian Journal of Physics, Vol. **57**, No. 4, pp. 207–217 (2017)

HETERO CuO_x/ZnO MICRO-/NANOSTRUCTURE: CARBOTHERMAL REDUCTION–VAPOUR PHASE TRANSPORT

A. Rahmati [a, b], F. Rahimi Bayaz [a, b], A. Lotfiani [c], and M. Kouhestani [d]

[a] *Department of Physics, Faculty of Science, Vali-e-Asr University of Rafsanjan, 7718897111 Rafsanjan, Iran*

[b] *Nanostructure Laboratory, Department of Physics, Faculty of Science, Vali-e-Asr University of Rafsanjan, 7718897111 Rafsanjan, Iran*

[c] *Laser and Plasma Research Institute, Shahid Beheshti University, P.O. Box 198396-3113, Evin, Tehran, Iran*

[d] *Physics Department, Payame Noor University, P.O. Box 19395-3697, Tehran, Iran*

Email: alirahmati1980@gmail.com

Received 10 April 2017; revised 19 May 2017; accepted 15 June 2017

ZnO micro-/nanostructures were synthesized by the carbothermal reduction–chemical vapour transport method. This work is focused on the effect of the substrate temperature and Cu catalyst layer on the shape and geometry of ZnO micro-/nanostructures. The thermally oxidized Cu template affects the structure, chemical identity, optical and photoluminescence properties of the ZnO micro-/nanostructure and results in a CuO_x/ZnO heterostructure. SEM studies give a direct evidence of the role of deposition temperature and Cu catalyst in the formation of a stable hemisphere based wire, a comb-like cantilever, a javelin-like tetrapod, a spherical and polyhedral cage of ZnO. XRD and Raman measurements confirm a hexagonal wurtzite structure of the ZnO micro-/nanostructure. The absorption edge of the ZnO/CuO_x heterostructure is redshifted in comparison to the pure ZnO structure. PL studies indicate that the UV emission can be suppressed significantly while the green emission is enhanced due to the change in the morphology of ZnO micro-/nanostructures.

Keywords: vapour phase transport growth, CuO_x/ZnO heterostructure, carbothermal reduction

PACS: 68.35.–p, 73.40.Kp, 81.16.–c

1. Introduction

ZnO micro-/nanostructures have attracted a great interest owing to their excellent properties and their potential applications as nanoscale electronic, photonic, field emission, sensing, energy conversion and piezoelectric devices [1–7]. Several strategies have been developed to synthesize ZnO micro-/nanostructures such as vapour-phase transport [8], metalorganic vapour-phase epitaxy [9], pulsed laser deposition [10], various wet-chemistry methods [5, 11], and magnetron sputtering [4, 12].

Various geometrical morphologies of ZnO micro-/nanostructures have been fabricated, such as rods [4, 5, 13], wires [8, 14, 15], tubes [16], combs [8], tetrapods [17], etc. However, the morphology and size control of ZnO micro-/nanostructures is still an issue and many groups have focused on this problem. Huang et al. [14] have suggested that the diameter of nanowires can be controlled by varying Au layer thickness and longer reaction times. Yao et al. [18] reported that the diameter of ZnO nanowires was temperature dependent and substrates placed in a low-temperature zone resulted in small diameters of ZnO nanowires. Wang et al. [19] suggested that the formation of nanotips and nanofinger arrays on two sides of a comb ribbon was a direct result of the surface polarity of ZnO. The polarity of the ZnO (0001) surface is the key enabling factor to determine micro-/nanostructures grown

on the surface. The self-catalysed process is likely a mechanism for the growth of oxide nanostructures without the presence of foreign metallic catalysts [19].

In the present study, the systematic size and shape control of different ZnO nanostructures (rods, wires, cages and combs) is demonstrated by carefully controlling the growth temperature, template and initial precursor. Morphology, dimensional control, structural, chemical bonding and optical characterizations, and discussion on the related growth mechanism are presented.

2. Experiment and methods

A horizontal one-side opened quartz tube (inner diameter 50 mm, length 100 cm) was placed inside a high-temperature tube furnace as shown in Fig. 1(a). The Cu template was deposited on a series of the cleaned polished Si substrate by thermal decomposition of copper (II) oxide as temperature raised above 650 °C. A mixture of high purity ZnO (99.999%) and activated carbon powders (mass ratio 1:2) was loaded at the end of a slender one-end sealed quartz tube (inner diameter 12 mm, length 20 cm). The copper island-coated silicon substrate was put into a small quartz tube as a collector (Fig. 1(a)). Then the small quartz tube with a reactive source and silicon or quartz substrate was placed into a bigger quartz tube and pushed to the centre of the furnace. The reactants were heated at 1100 °C. The temperature of the substrate region was lower than that of the reactants due to the temperature gradient, as shown in Fig. 1(b). After 2 h sintering, the small quartz tube was slowly cooled down to the room temperature in air and drawn out from the furnace. White and grayish-white colour products were formed on the surface of the silicon substrate.

The morphology of materials on the substrate was examined by a JEOL JSM-5910LV scanning electron microscope (SEM). X-ray diffractometry (XRD) patterns were obtained by a *Siemens* D5000 diffractometer using monochromatized Cu Kα radiation (λ = 1.5418 Å) under the accelerating voltage of 40 kV and the current of 40 mA with a normal θ–2θ scan. Raman spectra of the sample were measured by using a *Renishaw* micro-Raman System 1000 spectrometer with excitation from an Ar+ laser operating at 514.5 nm. Room-temperature PL was measured using a Hg lamp with an excitation wavelength of 365 nm.

3. Results and discussion

Figure 2 shows various morphology of pure ZnO and Cu templated ZnO (ZnO/CuO) structures on the Si substrate at different growth zones (or substrate temperatures). The pure micro-/nanostructure ZnO has a randomly columnar bone-like structure, a branched hemisphere, a comb-like cantilever and a random wire at different

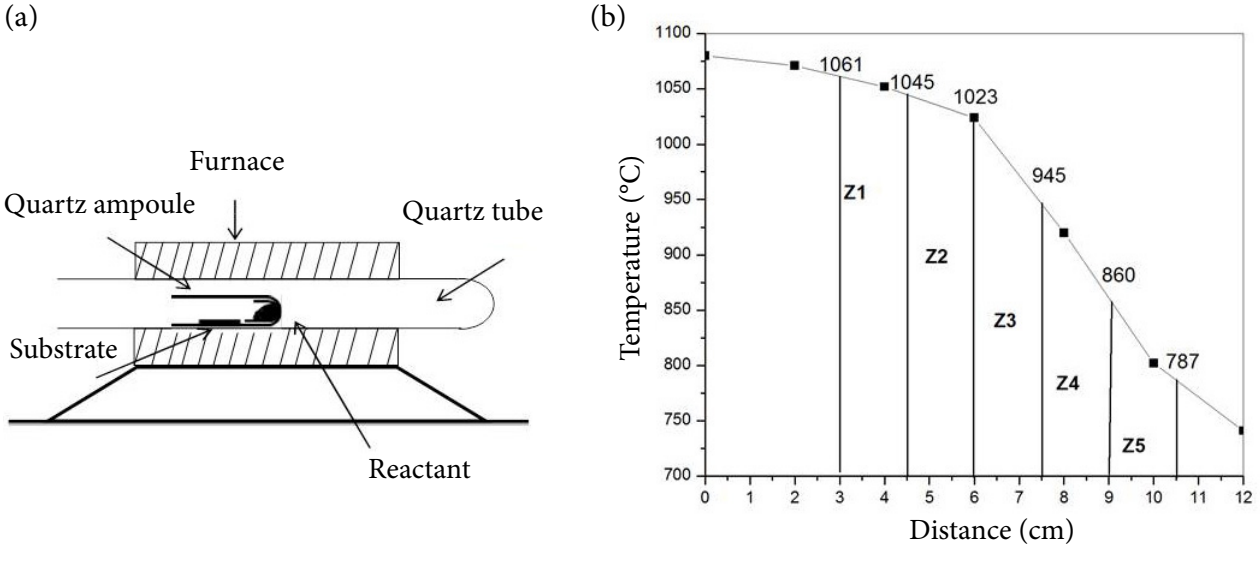

Fig. 1. Diagram of the furnace tube (a) and temperature profile of the furnace versus the distance between the substrate region and reactants (b). The temperature profile was measured using a 'K' type thermocouple.

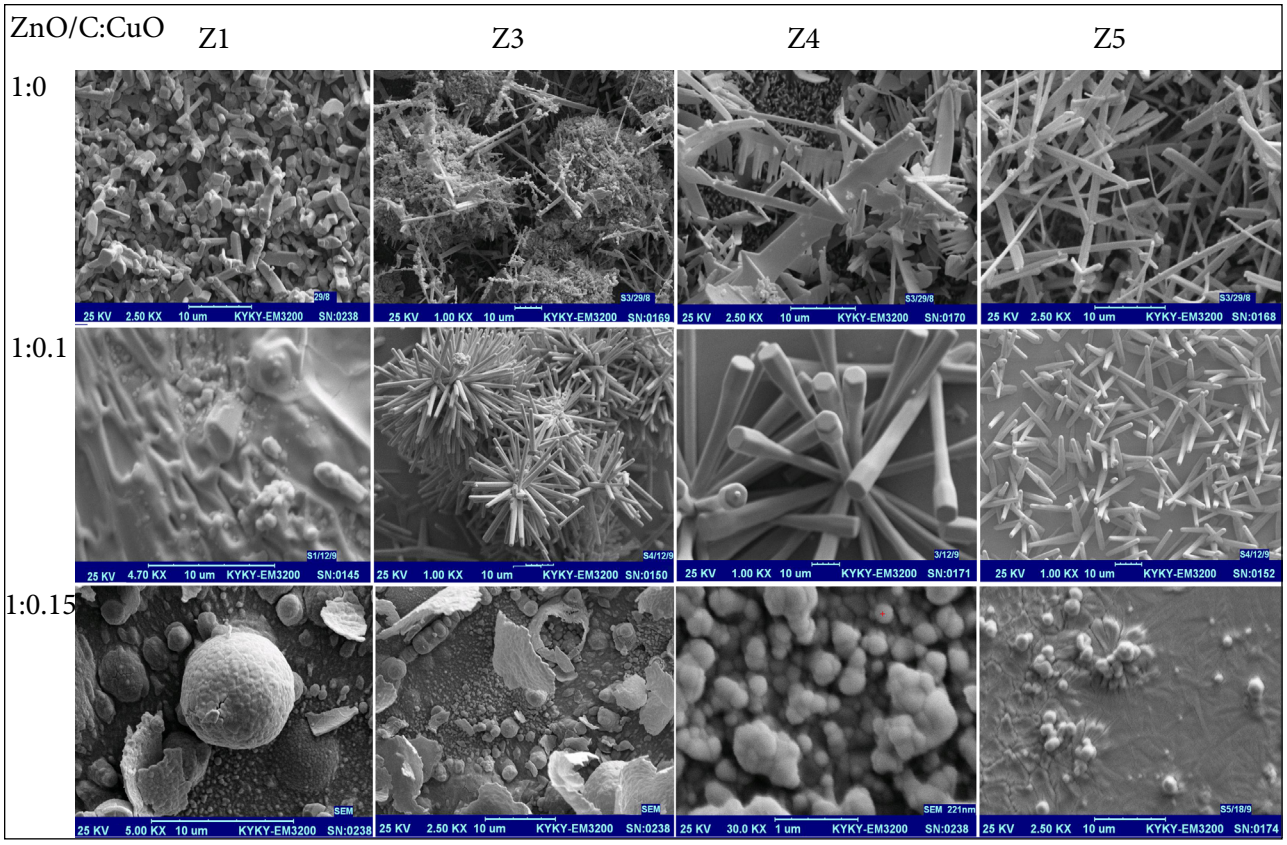

Fig. 2. Morphology of the pure ZnO and CuO_x template ZnO micro-/nanostructure on Si under different substrate temperature.

temperature zones Z1, Z3, Z4 and Z5, respectively. At the highest deposition temperature (Z1), the majority of the pure ZnO micro-/nanostructure consists of straight rods with a variable direction and diameter. Some of the rods merge together.

Hemisphere based wires (branched hemispheres) are formed with vapour condensation selectively on the concave tips between the branches where the chemical potential is lower than the convex and flat surface sites [20]. The comb-like cantilever of pure ZnO micro-/nanostructures is the result of surface polarization induced growth due to the chemically active (0001) Zn [19, 21]. The comb structures have comb teeth growing along [0001], the top/bottom surfaces being $\pm(0\bar{1}\bar{1}0)$ and the side surfaces $\pm(2\bar{1}\bar{1}0)$. The comb structure is an asymmetric growth along Zn [0001] [21]. The positively charged Zn^+ (0001) surface is chemically active and the negatively charged O^- $(000\bar{1})$ surface is relatively inert, resulting in growth of long fingers along [0001]. The Zn-terminated (0001) surface has tiny Zn clusters, which could lead to self-catalysed growth [21] without the presence of a foreign catalyst [21]. Anisotropic growth appears to be a common characteristic for the wurtzite family. A similar saw tooth growth has been observed for ZnS [22] and CdSe [23] and it is induced by Zn- and Cd-terminated (0001) surfaces, respectively. It was reported that ZnO wires might grow first along the [0001] direction, and then ultrafine nanoteeth might grow epitaxially along the $[11\bar{2}0]$ direction from the parent wires [21].

Finally, at the lowest deposition temperature (Z5), the ZnO micro-/nanostructure wires were randomly grown on the Cu nanoparticle deposited Si substrate. Therefore, the substrate distance from the source material and its temperature significantly affect the obtained morphology. This is most likely due to the variation in the rate of condensation (solidification) of ZnO species. The growth of the micro-/nanostructure is strongly dependent on the reactant (Zn and O_2), and therefore depends on the geometry of the experimental system, gas flow if any, as well as the type of the starting material.

Figure 2 also depicts the morphology of CuO templated ZnO (ZnO/CuO) micro-/nanostructures for the mass ratio of ZnO and C:Cu(II)O as 1:0.1 and 1:0.15. The substrate surface was covered with a metallic Cu layer above the temperature of 650 °C (Cu wetting). Hence, a substantial coalescence between the Cu layer and Zn vapour induces a special distribution of adsorbed Zn and consequently the shape control of the ZnO micro-/nanostructure during the growth process. Indeed, the Cu metal catalyst induces the formation of a multipod rod and a cage structure for the source nutrient of 1:0.1 and 1:0.15, respectively.

The morphology of ZnO/CuO (mass ratio 1:0.1) micro-/nanostructures is javelin-shaped tetrapods (tetrapods having trumpet like arms). As can be seen, these javelins have a perfect hexagonal geometry. The average diameter of the javelins is about 7.80 μm at the tip, and the average base diameter is 3.64 μm, with 40.42 μm in length. The orientation of the javelin growth is preferentially along the direction of the *c* axis ([0001]) because the *c* axis is perpendicular to the hexagonal plane [24].

The coalescence appears to depend on the thickness of the Cu layer or equivalently on the distance between Cu particles. To minimize the total surface energy, small Cu particles incline to aggregate and form larger particles via the coalescence, leading to the growth of ZnO nuclei. The average distance between two neighbouring ZnO nuclei decreases quickly when the Cu layer is thicker. To understand this coalescence between Zn vapours in the presence of Cu particles, one has to consider the high-temperature alloying process between Zn vapour and Cu particles. At the growth temperature ≥787 °C (Z5 in Fig. 1(b)), the increase in the size of alloy droplets and its surface diffusion can account for spatial distribution and relaxation of Zn vapour on the Cu template as a catalyst.

After the supersaturation is reached, Zn probably condenses out of the Cu–Zn alloy nuclei to form droplets. The size of the droplets is mainly determined by the global Zn vapour pressure in the furnace tube. To minimize the interface energy, the alloy nuclei tend to stay under the surface of these liquid-state Zn droplets. A very thin layer of Cu results in high density of Zn droplets.

These Zn droplets may make contact with each other and then merge into a continuous liquid-state network. Because the active Zn shows a large enthalpy of the formation of oxide [15], the interfacial interaction between the Zn and Cu template (layer) is strong. This layer is stable at the deposition temperature between 787–1061 °C and provides migration paths for the coalescence of Zn vapour in ambient air. In other words, the formation of a large scale metallic Cu layer occurs during the coalescence of Cu nuclei and facilitates the latter. As a result, larger Cu particles with a lower density are formed, which eventually leads to the growth of ZnO sites.

On the other hand, when the original Cu layer is thick, the Zn droplets are less likely to merge with each other to form a continuous layer owing to the fact that the barrier potential is larger. No continuous Zn layer is formed and Zn droplets remain separated throughout the whole process, leading to a rolled ZnO droplet (cage formation). Therefore, a liquid-state Cu layer determines the characteristics of the coalescent process and the size distribution of the grown ZnO shells or cages.

During the growth process in the presence of Cu catalysis, this transient liquid–metal layer gradually solidifies into separate ZnO geometries which terminate the migration and coalescence of Zu vapour. Naturally this ZnO layer emerges from the oxidized Zn rolled layer on top of the oxidized Cu template. There may be a close correlation between the ZnO coalescence and the formation of a continuous Cu buffer layer underneath the ZnO micro-/nanocages during the VLS growth. Such a buffer layer underneath the ZnO micro-/nanocages has not been reported previously, however, its role in the cage growth has not been elucidated so far. In contrast to the pure ZnO micro-/nanostructure, such buffer layer existed where the coalescent events were inhibited, and all ZnO micro-/nanocages grew directly on the Cu coated Si substrate [15].

Because the formation of a template layer underneath the ZnO micro-/nanostructure is critically important to distribute spatially the Zn vapour, the factors determining its onset and characteristics to form separate Zn droplets are the surface coverage of Cu islands on the substrate. Regarding the first factor, the effect of oxidation

competition between Zn droplets and Cu, different Cu layer thicknesses and the effect of Zn pressure demonstrate that they are also critical parameters.

By changing the composition of the source material from 1:0.1 to 1:0.15, ZnO cages have been grown. In the temperature zone of 1020–1060 °C, balls and polyhedra are observed; some of them are dispersed on the substrate and there appears to be no correlation among them, while some of them were formed in a higher temperature zone of typically 700–900 °C.

Figure 3 shows the X-ray diffraction pattern of a pure ZnO comb-like cantilever and a CuO templated ZnO javelin tetrapod and a polyhedral cage. The diffraction pattern of hexagonal wurtzite of the ZnO structure (JCPDS card No. 36-1451) with own related planes is observed for the pure ZnO comb-like cantilever. The diffraction peak intensity from the (101) plane has vanished from the sample deposited on the copper oxide template. The X-ray diffraction results indicate that the ZnO javelin and cage are grown with the *c* axis orientation on the CuO_x template. The dominant appearance of the (100) and (002) peaks of ZnO

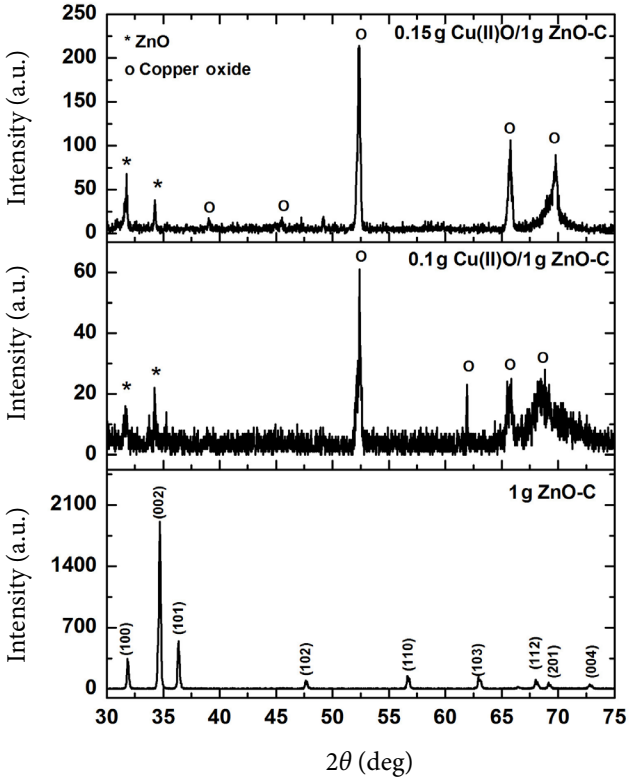

Fig. 3. XRD pattern of the ZnO–CuO_x structure with (a) 0, (b) 0.1 g and (c) 0.15 g Cu(II)O in nutrient materials.

shows its orientation relationship. The strong (002) peak of pure ZnO and ZnO/CuO_x (1:0.1) confirms the orientation of comb and javelin growth, respectively. Dominance of the (100) peak over the (002) peak for the source material of 1:0.15 confirms stopping of one-dimensional comb and rods growth along the (0001) direction and appearing of three-dimensional cage growth.

In a hexagonal structure, the lattice constant is calculated as [25]

$$\frac{1}{d_{hkl}} = \frac{4}{3}\left[\frac{h^2 + hk + k^2}{a^2}\right] + \frac{l^2}{c^2}. \quad (1)$$

Using the (100) and (002) reflections and the Bragg relation ($2d \sin\theta = \lambda$), *a* and *c* are calculated as

$$a = \sqrt{\frac{4}{3}}\frac{\lambda}{2\sin\theta_{100}} \quad (2a)$$

and

$$c = \frac{\lambda}{\sin\theta_{002}}, \quad (2b)$$

respectively. Cu enterance in the ZnO structure causes lattice expansion, because the Cu atomic radius (1.73 Å) is larger than that of Zn (1.67 Å) [4]. The ZnO lattice constant $a = 3.2478$ Å, $c = 5.2061$ Å [6]. As shown in the XRD pattern, the (002) peak is shifted towards the lower angle due to the Cu diffusion into the ZnO structure. This shift corresponds to an increase of the lattice constant. The calculated lattice constants are listed in Table 1. This dominant divalent state of Cu ions results from the strong Cu–O bonding in copper oxide, which also lowers the Cu solubility in ZnO. Hence, as seen from the XRD pattern, Cu segregates in copper oxide phases: monoclinic cupric CuO ($a = 4.6530$ Å, $c = 5.1080$ Å) and cubic cuprous Cu_2O ($a = 4.2520$ Å) [26]. The growth of CuO_x underneath the ZnO structure causes the lattice constants of ZnO to expand. It might be due to the lattice misfit (mismatch) between adjacent phases and subsequent lattice distortion.

The Zn–O bond length was calculated using [27]

$$l = \sqrt{\frac{a^2}{3} + \left(\frac{1}{2} - u\right)^2 c^2}, \quad (3)$$

where $u = \frac{a^2}{3c^2} + 0.25$ is the potential parameter of the hexagonal structure. The volume of a unit cell of the hexagonal system was calculated from Eq. [27]:

$$V = 0.866a^2c. \quad (4)$$

The out-of-plane and in-plane stress ($\sigma_{\perp,\square}$) in the ZnO plane can be determined by [28]

$$\begin{bmatrix}\sigma_{out}\\ \sigma_{in}\end{bmatrix} = -233\times10^9 \begin{bmatrix}(c_{bulk}-c)/c_{bulk}\\ (a_{bulk}-a)/a_{bulk}\end{bmatrix}, \quad (5)$$

where a and c are the lattice constants of the ZnO planes calculated from the X-ray diffraction data, a_{bulk} and c_{bulk} are the strain-free lattice parameters of ZnO. The negative sign of stress indicates that the stress is compressive for the ZnO comb-like structure (Table 1). The stress is tensile when the ZnO micro-/nanostructure is grown on the copper oxide template (Table 1). This increase of tensile stress is due to the lattice distortion produced around a Cu atom inside the Zn–Cu–O lattice and ZnO–CuO_x interface. The tensile stress persists and the lattices are distorted due to lower crystallinity. The calculated constant c/a ratio (1.6) shows that there is no change in the hexagonal wurtzite structure [25] caused by growth on the CuO_x template. The observed shift in the XRD peak position, the d-value, cell parameters, bond length, volume and stress confirm the distortion of the ZnO structure.

Raman spectroscopy gives information on the vibrational properties of ZnO micro-/nanostructures. In the hexagonal structures with C_{6v}^4 symmetry like ZnO, six sets of phonon normal modes at the Γ point (centre of the Brillouin zone) are optically active modes [7]. The phonons for wurtzite ZnO belong to the following irreducible representation:

$$\Gamma = A_1 + E_1 + 2B_1 + 2E_2. \quad (5)$$

The A_1 and E_1 modes are polar and split into transverse optical (TO) and longitudinal optical (LO) components. The E_2 modes are Raman active only. The B_1 modes are infrared and Raman inactive or silent modes. It is known that the E_2 (low) mode in ZnO is associated with the vibration of the heavy Zn sub-lattice and the E_2 (high) mode involves only oxygen atoms.

The E_2 (high) mode is characteristic of the wurtzite phase [29]. Figure 4 shows the Raman spectrum of CuO_x templated ZnO along with the spectrum of the pure ZnO for comparison. They are clearly indicative of a good wurtzite structure of the pure and ZnO/CuO_x material. From Fig. 4 one observes the effect of the CuO_x template on the E_2 (high) mode of ZnO since its intensity decreases. The Raman signal indicates peaks at 446 and 444 cm^{-1} for the pure ZnO and

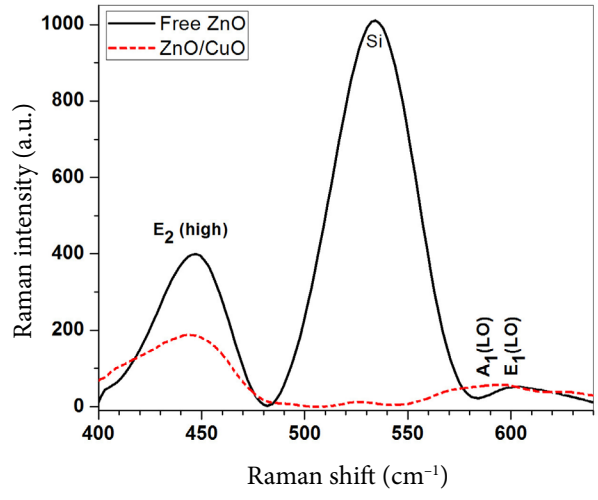

Fig. 4. Raman spectra of the pure ZnO and ZnO/CuO_x structure.

Table 1. The observed shift in the XRD peak position, cell parameters, bond length, cell volume and out- and in-plane stress in the ZnO comb, javelin and cage.

CuO:ZnO	2θ (deg)	(hkl)	a (Å)	c (Å)	Bond length (Å)	Volume V (Å³)	Out-of-plane stress $\sigma_\perp$ (GPa)	In-plane stress σ_μ (GPa)
0:1	31.8235 34.6941	(100) (002)	3.2470	5.1711	1.9724	47.2134	–1.5664	–0.0574
0.1:1	31.7412 34.2470	(100) (002)	3.2551	5.2365	1.9836	48.0494	1.3606	0.5237
0.15:1	31.6706 34.2470	(100) (002)	3.2622	5.2365	1.9865	48.2592	1.3606	1.0331

ZnO/CuO_x material that shifted in the signal at ~437 cm^{-1} for the ZnO micro-/nanostructure, which was also shifted in comparison to the Raman signal at ~437 cm^{-1} for the ZnO micro-/nanostructure grown by other techniques [30]. The Raman line of the E_2 (high) mode becomes broad and weaker, which means that the wurtzite crystalline structure of ZnO is weakened by high CuO_x templating and due to the formation of complex defects $[Cu_{Zn}–Zn_i]^x$ in the CuO_x–ZnO interface. The frequency shift was explained by alloy potential fluctuation (APF) using the spatial correlation model by Samanta et al. [31].

The intense peak near 439 cm^{-1} due to the E_2 (high) mode displays a clear asymmetry toward low frequencies. The asymmetric line shape has been successfully explained and analysed by Cusco et al. [32], in terms of resonant anharmonic interaction of the high-E_2 mode with a band of combined transverse and longitudinal acoustic modes, as the steep variation of the two-phonon density of states around the high-E_2 frequency leads to a distorted phonon line shape. Mixing of two different cations through doping in a solid solution could affect the local polarizability by charge distribution and result in at least one vibrational mode being strongly influenced [33].

In addition to the XRD pattern of pure ZnO and ZnO/CuO_x, high-E_2 frequency in Raman spectra confirms the formation of a ZnO hexagonal wurtzite structure. As shown in Fig. 4, there is no significant difference in the Raman spectra of the pure ZnO and ZnO/CuO_x heterostructure. The lower Raman peak in the ZnO/CuO_x heterostructure in comparison to that of the pure ZnO is related to a lower crystallinity that is in agreement with the XRD pattern.

Figure 5 depicts the variation of the bandgap energy of pure ZnO and ZnO/CuO_x heterostructure absorption spectra. The CuO_x template and the distribution of Cu species during nucleation growth cause changes in the shape of ZnO from a teeth-like structure to a javelin and, finally, a cage structure. On the other hand, the band-edge of ZnO/CuO_x is redshifted in comparison to the pure micro-/nanostructure. It is worthwhile to notice that the bandgap shrinkage of the ZnO/CuO_x heterostructure cannot be substantially dependent on the morphology of the ZnO micro-/nanostructure. But the CuO_x template significantly causes the bandgap to reduce. Depending on the processing parameters during deposition, copper oxide can exist in two crystalline phases with p-type conductivity: a cuprous oxide (Cu_2O) cubic structure with a direct band gap range of 2.1–2.6 eV and a cupric oxide (CuO) monoclinic structure with a direct band gap of 1.3–2.1 eV. These oxides exhibit a high absorption coefficient in the visible region and can be grown by a variety of techniques [4, 12]. The out-plane and in-plane stress (Table 1) can provide another mechanism to bandgap narrowing.

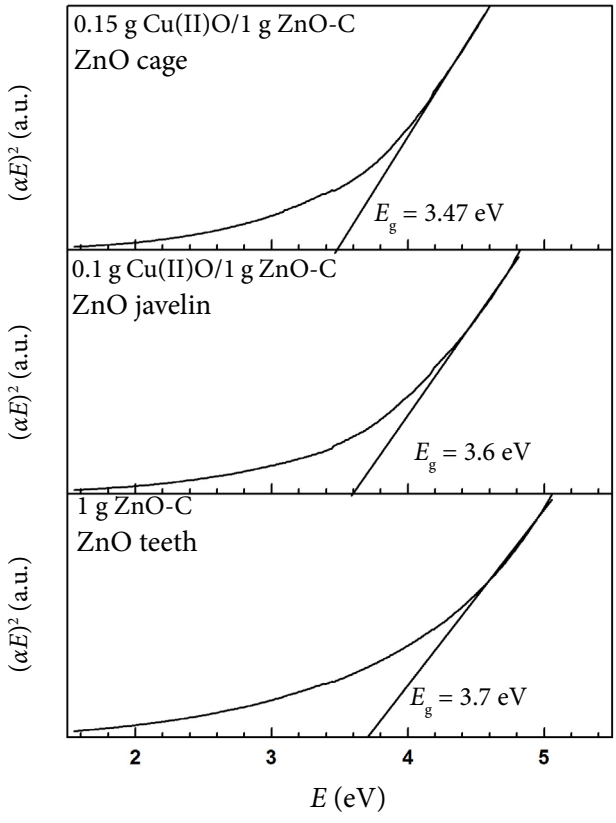

Fig. 5. Absorption spectrum of (a) the pure ZnO teeth, (b) the ZnO javelin on the CuO_x template with 0.1 g and (c) the ZnO cage on the CuO_x template with 0.15 g Cu(II)O in nutrient materials.

3.3.4. Photoluminescence study

Figure 6(a) shows the PL spectrum of ZnO branched hemisphere and comb-like cantilever structures. The branched hemisphere has only a green emission around 545 nm, but the comb-like cantilever has two emitting bands including a UV emission at around 393 nm and as well as

a green band around 521 nm. The comb-like cantilever structure exhibits near-band-edge emission (NBE), in comparison to the branched hemisphere structure, due to a good crystalline quality in the comb-like cantilever [34]. The difference between the green emission from the comb-like cantilever and the branched hemisphere structures is related to defect concentration.

It has been suggested that the green band emission corresponds to the singly ionized oxygen vacancy in ZnO and results from the recombination of a photogenerated hole with the singly ionized charge state of this defect. The stronger the intensity of the green luminescence is, the more singly ionized oxygen vacancies are [21, 35]. For the green emission, though a number of hypotheses have been proposed, some assignments are highly controversial. Typical works reported that the transitions might occur between singly ionized oxygen vacancies and photoexcited holes, or electrons close to the conductive band and deeply trapped holes at V_O^{2+} antisite oxygen, zinc interstitials, zinc vacancies, etc. [35, 36]. The yellow-orange band emission is attributed to the oxygen interstitial defects located in the bulk [35, 36].

Figure 6(b) shows the PL spectrum of the ZnO javelin-like tetrapod and curved tip rod structures. The ZnO javelin-like tetrapod structure has only a green emission around 523 nm. The ZnO curved tip rod structures have three emitting bands, including a strong ultraviolet emission-excitonic recombination at around 388 nm, a blue band (486 nm) as well as a green band (523 nm) observed. The UV emission must be contributing to the near band edge emission of the wide band-gap ZnO. The observation of the blue band emission

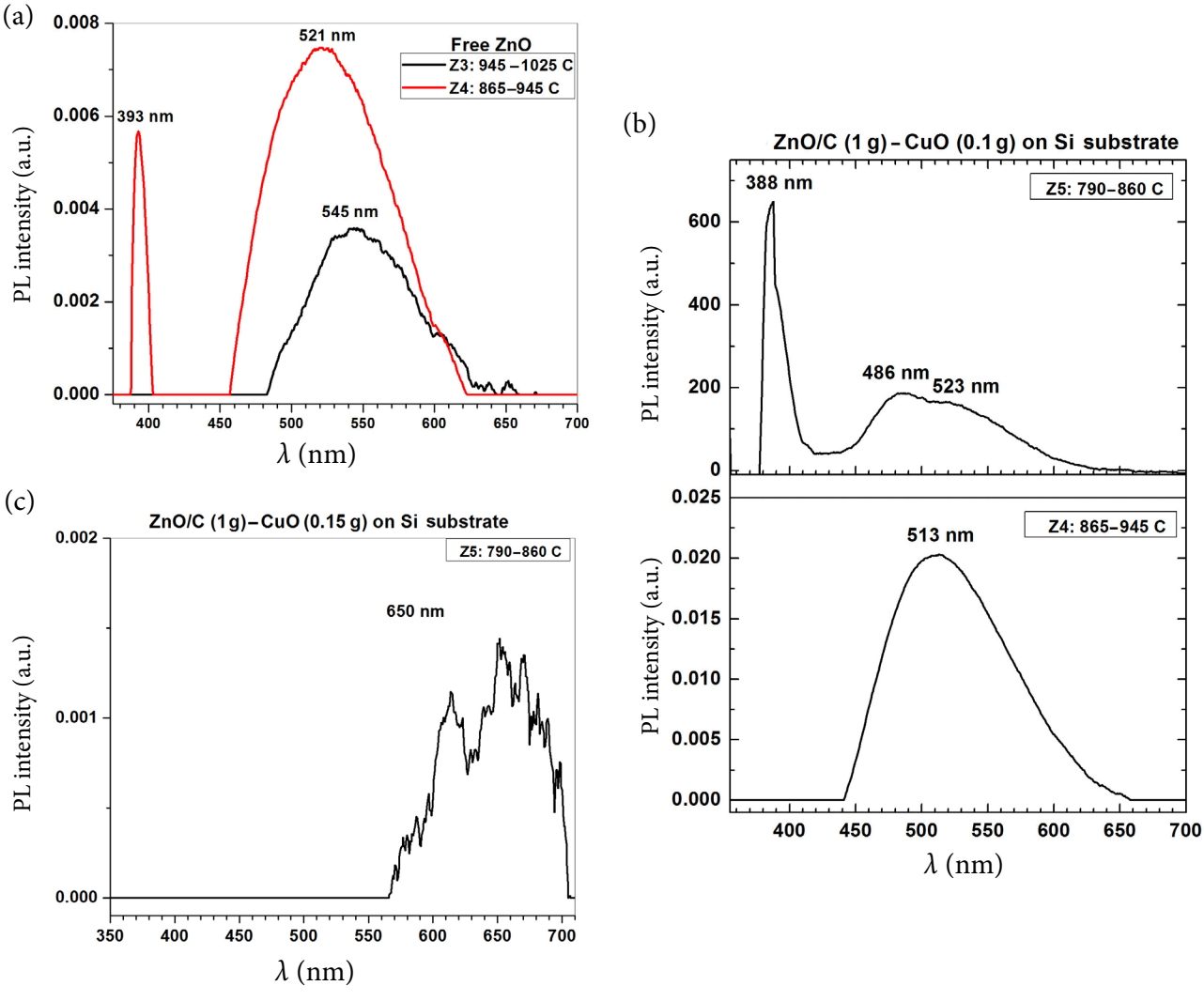

Fig. 6. Absorption spectrum of (a) the pure ZnO teeth and the CuO_x templated ZnO with (b) 0.1 g and (c) 0.15 g Cu(II)O in nutrient materials.

(486 nm) of the ZnO film has also been reported [21], using cathodoluminescence. Figure 6(c) also depicts a weak red emission of the ZnO polyhedral cage around 650 nm, which may be attributed to the contribution of Cu template oxidation.

4. Conclusions

ZnO/CuO_x hetero-micro-/nanostructures were synthesized by the carbothermal reduction–chemical vapour transport method. This work is focused on tuning the shape and geometry of the ZnO micro-/nanostructure to the substrate temperature, Cu catalyst layer. The thermally oxidized Cu template underneath the ZnO structure (ZnO/CuO_x heterostructure) affects its structure and chemical identity, optical and photoluminescence properties. A stable hemisphere based wire, a comb-like cantilever, a javelin-like tetrapod, a spherical and polyhedral cage of a hexagonal wurtzite structure of the ZnO micro-/nanostructure are formed depending on the deposition condition. The absorption edge of the ZnO/CuO_x heterostructure is redshifted in comparison to the pure ZnO structure. It is possible to tune the PL spectra from green to UV and, finally, red emission by growth temperature and precursor composition.

Acknowledgements

The authors would like to acknowledge the financial support of the Iranian Nanotechnology Initiative. Ali Rahmati (the corresponding author) is grateful to Dr. Masoud Karimipour and Dr. Mehdi Molaei for fruitful discussions.

References

[1] Z. Zhang, S.J. Wang, T. Yu, and T. Wu, Controlling the growth mechanism of ZnO nanowires by selecting catalysts, J. Phys. Chem. C **111**, 17500–17505 (2007).

[2] M. Laurenti, S. Stassi, M. Lorenzoni, M. Fontana, G. Canavese, V. Cauda, and C.F. Pirri, Evaluation of the piezoelectric properties and voltage generation of flexible zinc oxide thin films, Nanotechnology **26**, 215704 (2015).

[3] M. Laurenti, G. Canavese, A. Sacco, M. Fontana, K. Bejtka, M. Castellino, C.F. Pirri, and V. Cauda, Nanobranched ZnO structure: p-type doping induces piezoelectric voltage generation and ferroelectric-photovoltaic effect, Adv. Mater. **27**, 4218–4223 (2015).

[4] A. Rahmati and S. Zakeri Afshar, Heteroepitaxial ZnO/CuO thin film and nanorods array: photoconductivity and field emission effect, J. Mater. Sci. Mater Electron. **28**, 13032 (2017), https://doi.org/10.1007/s10854-017-7135-8

[5] A. Rahmati and M. Yousefi, Well oriented ZnO nanorods arrray: negative resistance and optical switching, Z. Anorg. Allg. Chem. **643**, 870–876 (2017).

[6] Ü. Özgür, Ya. I. Alivov, C. Liu, A. Teke, M.A. Reshchikov, S. Doğan, V. Avrutin, S.-J. Cho, and H. Morkoç, A comprehensive review of ZnO materials and devices, J. Appl. Phys. **98**, 041301 (2005).

[7] H. Morkoç and Ü. Özgür, in: *Zinc Oxide, Fundamentals, Materials and Device Technology* (Wiley VCH, 2009).

[8] U. Manzoor and D.K. Kim, Size control of ZnO nanostructures formed in different temperature zones by varying Ar flow rate with tunable optical properties, Physica E **41**, 500–505 (2009).

[9] W.I. Park, D.H. Kim, S.W. Jung, and G.C. Yi, Metalorganic vapour-phase epitaxial growth of vertically well-aligned ZnO nanorods, Appl. Phys. Lett. **80**, 4232 (2002).

[10] A.B. Hartanto, X. Ning, Y. Nakata, and T. Okada, Growth mechanism of ZnO nanorods from nanoparticles formed in a laser ablation plume, Appl. Phys. A **78**, 299 (2004).

[11] L. Vayssieres, K. Keis, S.E. Lindquist, and A.J. Hagfeldt, Purpose-built anisotropic metal oxide material: 3D highly oriented microrod array of ZnO, Phys. Chem. B **105**, 3350 (2001).

[12] C.R. Gobbiner, A.V. Muhammed Ali, and D. Kekuda, CuO/ZnO planar bilayer heterojunction grown by reactive dc magnetron sputtering, J. Mater. Sci. Mater. Electron. **26**, 9801–9807 (2015).

[13] Y.W. Heo, V. Varadarajan, M. Kaufman, K. Kim, D.P. Norton, F. Ren, and P.H. Fleming, Site-specific growth of ZnO nanorods using catalysis-

driven molecular-beam epitaxy, Appl. Phys. Lett. **81**(16), 3046–3048 (2002).

[14] M.H. Huang, Y. Wu, H. Feick, N. Tran, E. Weber, and P. Yang, Catalytic growth of zinc oxide nanowires by vapour transport, Adv. Mater. **13**(2), 113–116 (2001).

[15] D.L. Guo, X. Huang, G.Z. Xing, Z. Zhang, G.P. Li, M. He, H. Zhang, H.Y. Chen, and T. Wu, Metal-layer-assisted coalescence of Au nanoparticles and its effect on diameter control in vapour-liquid-solid growth of oxide nanowires, Phys. Rev. B **83**, 045403 (2011).

[16] G.W. She, X. Huang, L.L. Jin, X.P. Qi, L. Mu, and W.S. Shi, Electrochemical sensors: SnO_2 nanoparticle-coated ZnO nanotube arrays for high-performance electrochemical sensors, Small **10**(22), 4685–4692 (2014).

[17] F.M. Li, G.W. Hsieh, S. Dalal, M.C. Newton, J.E. Stott, P. Hiralal, A. Nathan, P.A. Warburton, H.E. Unalan, P. Beecher, A.J. Flewitt, I. Robinson, G. Amaratunga, and W.I. Milne, Zinc oxide nanostructures and high electron mobility nanocomposite thin film transistors, IEEE Trans. Electron Dev. **55**(11), 3001 (2008).

[18] B.D. Yao, Y.F. Chan, and N. Wang, Formation of ZnO nanostructures by a simple way of thermal evaporation, Appl. Phys. Lett. **81**, 757 (2002).

[19] Z.L. Wang, X.Y. Kong, and J.M. Zuo, Induced growth of asymmetric nanocantilever arrays on polar surfaces, Phys. Rev. Lett. **91**, 185501 (2003).

[20] G. Modi, Zinc oxide tetrapod: a morphology with multifunctional applications, Adv. Nat. Sci. Nanosci. Nanotechnol. **6**, 033002 (2015).

[21] Z.L. Wang, Zinc oxide nanostructures: growth, properties and applications, J. Phys. Condens. Matter **16**, R829–858 (2004).

[22] D. Moore, C. Ronning, C. Ma, and Z.L. Wang, Wurtzite ZnS nanosaws produced by polar surfaces, Chem. Phys. Lett. **385**, 8 (2004).

[23] C. Ma, Y. Ding, D. Moore, X.D. Wang, and Z.L. Wang, Single-crystal CdSe nanosaws, J. Am. Chem. Soc. **126**, 708 (2004).

[24] R. Yousefi, F. Jamali-Sheini, A. Khorsand Zak, and M.R. Mahmoudian, Effect of indium concentration on morphology and optical properties of In-doped ZnO nanostructures, Ceram. Int. **38**, 6295–6301 (2012).

[25] B.D. Cullity, *Elements of X-ray Diffractions* (Addison-Wesley, Reading, MA, 1978).

[26] S.W. Lee, Y.S. Lee, J.Y. Heo, S.C. Siah, D. Chua, R.E. Brandt, S.B. Kim, J.P. Mailoa, T. Buonassisi, and R.G. Gordon, Improved Cu_2O-based solar cells using atomic layer deposition to control the Cu oxidation state at the p-n junction, Adv. Energy Mater. **4**(11), 1301916 (2014).

[27] G. Srinivasan, R.T.R. Kumar, and J. Kumar, Li doped and undoped ZnO nanocrystalline thin films: a comparative study of structural and optical properties, J. Solgel Sci. Technol. **43**, 171–177 (2007).

[28] O. Lupan, T. Pauporte, L. Chow, B. Viana, F. Pelle, L.K. Ono, B.R. Cuenya, and H. Heinrich, Effects of annealing on properties of ZnO thin films prepared by electrochemical deposition in chloride medium, Appl. Surf. Sci. **256**, 1895–1907 (2010).

[29] O. Lupan, L. Chow, L.K. Ono, B. Roldan Cuenya, G. Chai, H. Khallaf, S. Park, and A. Schulte, Synthesis and characterization of Ag- or Sb-doped ZnO nanorods by a facile hydrothermal route, J. Phys. Chem. C **114**, 12401–12408 (2010).

[30] P.K. Sharma, R.K. Dutta, and A.C. Pandey, Doping dependent room-temperature ferromagnetism and structural properties of dilute magnetic semiconductor ZnO: Cu^{2+} nanorods, J. Magn. Magn. Mater. **321**, 4001–4005 (2009).

[31] K. Samanta, P. Bhattacharya, R.S. Katiyar, W. Iwamoto, P.G. Pagliuso, and C. Rettori, Raman scattering studies in dilute magnetic semiconductor $Zn_{1-x}Co_xO$, Phys. Rev. B **73**, 245213 (2006).

[32] R. Cusco, E. Alarcon-Llado, J. Ibanez, L. Artus, J. Jimenez, B. Wang, and M. Callahan, Temperature dependence of Raman scattering in ZnO, Phys. Rev. B **75**, 165202 (2007).

[33] X.F. Wang, J.B. Xu, X.J. Yu, K. Xue, and X. Zhao, Structural evidence of secondary phase segregation from the Raman vibrational modes in $Zn_{1-x}Co_xO$ ($0<x<0.6$), Appl. Phys. Lett. **91**, 031908 (2007).

[34] M. Karaliunas, T. Serevicius, E. Kuokstis, S. Jursenas, S.Y. Ting, J.J. Huang, and C.C. Yang,

Optical characterization of MBE-grown ZnO epilayers, Adv. Mat. Res. **222**, 86–89 (2011).

[35] D.D. Wang, G.Z. Xing, J.H. Yang, L.L. Yang, M. Gao, J. Cao, Y.J. Zhang, and B. Yao, Dependence of energy transfer and photoluminescence on tailored defects in Eu-doped ZnO nanosheets-based microflowers, J. Alloy. Comp. **504**, 22–26 (2010).

[36] G.Z. Xing, G.C. Xing, M.J. Li, E.J. Sie, D. Wang, A. Sulistio, Q.L. Ye, C. Hon, A. Huan, T. Wu, and T.C. Sum, Charge transfer dynamics in Cu-doped ZnO nanowires, Appl. Phys. Lett. **98**, 102105 (2011).

ĮVAIRIALYTIS CuO_x/ZnO MIKRO- ARBA NANODARINYS: KARBOTERMINĖ REDUKCIJA SU GARŲ FAZĖS PERNAŠA

A. Rahmati [a, b], F. Rahimi Bayaz [a, b], A. Lotfiani [c], M. Kouhestani [d]

[a] *Rafsandžano Vali-e-Asr universiteto Mokslo fakulteto Fizikos katedra, Rafsandžanas, Iranas*

[b] *Rafsandžano Vali-e-Asr universiteto Mokslo fakulteto Nanostruktūrų laboratorija, Rafsandžanas, Iranas*

[c] *Šahid Behešti universitetas, Evinas, Teheranas, Iranas*

[d] *Pajam Nur universitetas, Teheranas, Iranas*